

Causes of ferroelectricity in HfO₂-based thin films: An *ab initio* perspective

Mehmet Dogan^{*1,2,3,4}, Nanbo Gong^{1,5}, Tso-Ping Ma^{1,5} and Sohrab Ismail-Beigi^{1,2,6,7}

¹*Center for Research on Interface Structures and Phenomena,
Yale University, New Haven, Connecticut 06520, USA*

²*Department of Physics, Yale University,
New Haven, Connecticut 06520, USA*

³*Department of Physics, University of California,
Berkeley, California 94720, USA*

⁴*Materials Science Division,
Lawrence Berkeley National Laboratory,
Berkeley, California 94720, USA*

⁵*Department of Electrical Engineering, Yale University,
New Haven, Connecticut 06520, USA*

⁶*Department of Applied Physics, Yale University,
New Haven, Connecticut 06520, USA*

⁷*Department of Mechanical Engineering and Materials Science,
Yale University, New Haven, Connecticut 06520, USA*

^{*}*Corresponding author: mhmtdogan@gmail.com*

(Dated: April 1, 2019)

We present a comprehensive first principles study of doped hafnia in order to understand the formation of the ferroelectric orthorhombic [001] grains. Assuming that tetragonal grains are present during the early stages of growth, matching plane analysis shows that tetragonal [100] grains can transform into orthorhombic [001] during thermal annealing, when they are laterally confined by other grains. We show that among 0%, 2% and 4% Si doping, 4% doping provides the best conditions for the tetragonal [100] \rightarrow orthorhombic [001] transformation. This also holds for Al doping. We also show that for Hf_xZr_{1-x}O₂, where we have studied $x = 1.00, 0.75, 0.50, 0.25, 0.00$, the value $x = 0.50$ provides the most favorable conditions for the desired transformation. In order for this transformation to be preferred over the tetragonal [100] \rightarrow monoclinic [100] transformation, out-of-plane confinement also needs to be present, as supplied by a top electrode. Our findings illuminate the mechanism that causes ferroelectricity in hafnia-based films and provide an explanation for common experimental observations for the optimal ranges of doping in Si:HfO₂, Al:HfO₂ and Hf_xZr_{1-x}O₂. We also present model thin film heterostructure computations of Ir/HfO₂/Ir stacks in order to isolate the interface effects, which we show to be significant.

I. INTRODUCTION

Achieving ferroelectricity in thin films has been a decades-long research endeavor because of potential technological applications, e.g., the ferroelectric field effect transistors (FEFET) and ferroelectric random-access memory (FERAM) [1–4]. The ferroelectric-based technology provides tremendous advantages over the dominant non-volatile memory technology, such as low power consumption, controllability over variability, and fast switching speed. However, this promising technology has not been widely implemented due to the lack of ferroelectric materials that fulfill the all of the requirements for a viable memory technology: scalability, CMOS compatibility, and memory retention [5, 6]. HfO₂ is one of the most widely used dielectric gate oxides in today's field effect transistor devices [7]. Most importantly, it is thermodynamically stable on silicon up to high temperatures, allowing abrupt HfO₂/Si interfaces to be grown without formation of silica in the interfacial region [8]. In addition, with a large band gap of 5.3 - 5.7 eV and a dielectric constant of $\epsilon_r \approx 20$ in its bulk form under ordinary conditions [9], HfO₂ is a widely used gate insulator and a re-

placement material for SiO₂ [10]. The recent discovery of ferroelectricity in HfO₂-based thin films has further multiplied the research interest in this material [11, 12]. It has been shown in various experimental studies that ferroelectricity in HfO₂-based films arises from the creation of the polar orthorhombic phase (space group: Pca2₁) of HfO₂ during a rapid annealing process in conjunction with the presence of a capping electrode (typically TiN). It has also been demonstrated that the ferroelectric properties of these films strongly depend on factors such as the doping species, doping concentration, annealing temperature and film thickness [9, 13]. Even though HfO₂-based ferroelectric memory have been experimentally demonstrated using various conditions, a systematic microscopic understanding of the effects of the aforementioned factors is presently lacking. This is, in part, due to the polycrystalline and complex nature of the HfO₂ films that have been grown to date, and in part, due to the relatively new interest in this field.

To the best of our knowledge, the ferroelectric hafnia-based thin films are polycrystalline and contain differently oriented grains of monoclinic (space group: P2₁/s), tetragonal (P4₂/nmc) and orthorhombic (Pca2₁) phases

in various ratios. The monoclinic and the tetragonal phases are non-polar, and they are the observed bulk phases of HfO_2 at room temperature and at high temperature, respectively [14, 15]. Experiments demonstrate that the orthorhombic phase arises during the rapid annealing with a capping electrode. In addition, the concentration of dopants is crucial in determining the ferroelectric properties. Because the volume fraction of the orthorhombic phase compared to the other non-polar phases is what ultimately decides the robustness of ferroelectricity in the HfO_2 films, a structural understanding of the favorable conditions for this phase is crucial in order to optimize the growth procedure.

To this end, in our *ab initio* studies we investigate the energetics of different phases of HfO_2 with varying amounts of Si and Zr doping and subject to a range of epitaxial strain states. In Section §II we summarize our knowledge of the experimental findings on ferroelectric thin films of hafnia to date. After describing our methods in §III, we move on to our computational study of doping and strain on hafnia with a particular focus on Si:HfO_2 and $\text{Hf}_x\text{Zr}_{1-x}\text{O}_2$ in Section §IV. We have found that at certain doping levels the transformation of the high temperature tetragonal phase to the out-of-plane polarized orthorhombic phase is favored. These results, together with additional analysis, help explain the common experimental observations as well as some of the underlying causes from a microscopic viewpoint. We also describe, in Section §IV, results on simulated HfO_2 thin films including the interface with electrodes in order to obtain some insight on the energetics of interfacial and surface effects in thin films.

II. SUMMARY OF EXPERIMENTS TO DATE

Since their discovery in 2011, ferroelectric hafnia thin films have garnered tremendous experimental attention. In Table I we list some of the studies that have investigated factors such as doping species, doping concentration, thickness of the film, and top and bottom electrodes (TE/BE).

These studies have generally found that, when the HfO_2 films are doped with a few percent of a wide range of dopants or with $\sim 50\%$ Zr, grown to be $\sim 5 - 20$ nm thick between two metal electrodes, and annealed at $\sim 800 - 1000$ °C, they can display ferroelectricity. Some of the studies [11, 16, 17, 21] have shown that for $\text{TiN/HfO}_2/\text{TiN}$ stacks, if the film is annealed before the deposition of the top electrode, then the ferroelectric behavior is significantly suppressed, which indicates that the confinement provided by the top electrode during annealing is crucial for ferroelectricity.

In terms of the atomic structure of the films, many of these studies have performed XRD analyses to show that ferroelectricity is intimately related to the presence of the

Ref.	Dopant	TE/BE	d (nm)	Observations
Böscke et al. [11]	Si	TiN/TiN	7-10	FE at 2.6%-4.3% Si; \sim AFE at 5.6% Si.
Müller et al. [16]	Y	TiN/TiN	10	FE at 2.3%-5.2% Y.
Mueller et al. [17]	Al	TiN/TiN	16	FE at 4.8% Al; AFE at 8.5% Al.
Müller et al. [12]	Zr	TiN/TiN	9	PE at $<30\%$ Zr; FE at $\sim 30\%$ Zr; AFE at $>70\%$ Zr.
Yurchuk et al. [18]	Si	TiN/TiN	9, 27	FE at 4.4% Si, 9 nm; \sim PE at 27 nm.
Park et al. [19]	50% Zr	TiN/TiN	5-25	FE at 5-17 nm; PE at 25 nm. Pca ₂₁ phase confirmed.
Park et al. [20]	50% Zr	TiN/TiN, TiN/Pt	5-27	FE at 8-19 nm for TiN; Less FE for Pt at 8 nm; PE for Pt at >13 nm.
Lomenzo et al. [21]	Si	TiN/Si, Ir/Si, Ir/Ir	10	FE similar for TiN/Si and Ir/Si. Smaller P_r for Ir/Ir.
Schroeder et al. [22]	Si, Al, Y, Gd, La, Sr	TiN/TiN	10	FE at 4.4% Si; AFE at $>5.6\%$ Si. Similar for Al. No AFE for other dopants.
Park et al. [23]	50% Zr	TiN/TiN, TiN/Ir	9-24	FE at 9-19 nm for TiN; FE at 12-15 nm for Ir.
Sang et al. [24]	Gd	TiN/TiN	27	FE; Pca ₂₁ phase confirmed.
Hoffmann et al. [25]	Gd	TiN/TiN, TiN/TaN, TaN/TaN	10-27	FE similar for all stacks; TaN/TaN $>$ TiN/TiN \simeq TiN/TaN in terms of P_r .
Chernikova et al. [26]	50% Zr	TiN/TiN	2.5	FE; Pca ₂₁ phase confirmed.
Park et al. [27]	Al, Gd	TiN/TiN	10	FE at 5.7%-6.9% Al, 3.0%-3.9% Gd; PE at 8.8% Al.
Park et al. [28]	Si	TiN/TiN	10, 40	FE at 3.8%-5.6% Si, 10 nm; \sim PE at 4.5% Si, 40 nm; PE at 5.0%-6.3% Si, 40 nm.

Table I. Selected experimental studies of ferroelectric hafnia thin films published between 2011 and 2018, listed chronologically. PE means paraelectric, FE means ferroelectric, AFE means antiferroelectric.

orthorhombic $Pca2_1$ phase of HfO_2 . The path to the stabilization of this phase is believed to be via the creation of grains of the tetragonal $P4_2/nmc$ phase which are present when the film is first deposited [12]. The tetragonal phase is known to be stabilized by surface effects [29], and recent studies have shown doping to be a stabilizer for this phase as well [30, 31]. Hence, it appears that for ferroelectric hafnia-based films, the orthorhombic phase is obtained from the tetragonal grains during rapid thermal annealing under the confinement of a top electrode. Crystallization without a top electrode leads to the formation of the monoclinic $P2_1/s$ phase, which is the non-polar ground state at relevant temperatures. The causes for the favorability of the tetragonal \rightarrow orthorhombic transition over the tetragonal \rightarrow monoclinic transition under these doping/thickness/temperature/confinement conditions are not well understood.

III. COMPUTATIONAL METHODS

We compute minimum energy structures using density functional theory (DFT) in the Perdew–Burke–Ernzerhof Generalized Gradient Approximation (PBE GGA) [32] with ultrasoft pseudopotentials [33]. We use the QUANTUM ESPRESSO software package [34]. Plane wave energy cutoffs of 55 Ry and 35 Ry are used for bulk and thin film simulations, respectively. We sample the Brillouin zone with an $8 \times 8 \times 8$ Monkhorst–Pack k -point mesh (per 12 atom unit cells) and a 0.02 Ry Marzari–Vanderbilt smearing [35] for bulk samples; slab (thin film) systems are sampled with a $6 \times 6 \times 1$ mesh. For thin film simulations, periodic copies of the slab are separated by $\sim 12 \text{ \AA}$ of vacuum in the z -direction (see Figure 1 for a representative unit cell), and the in-plane lattice constants of the slab are fixed to the computed bulk lattice constants of HfO_2 for the plane under consideration. In general, a slab may have an overall dipole moment that can artificially interact with its periodic copies through the vacuum gap. We eliminate this effect by introducing a fictitious dipole in the vacuum region of the cell which cancels out the electric field in vacuum [36]. All atoms are relaxed until the forces on the atoms are less than 10^{-4} Ry/Bohr in magnitude along all axial directions. We use both direct substitution of atoms as well as the virtual crystal approximation (VCA) to model doping [37]. In the VCA, to approximate the mixing of two elements A and B with ratios x and $1-x$, a virtual element is created by linearly interpolating the pseudopotentials of A and B such that the resulting pseudopotential is $V = xV_A + (1-x)V_B$. The VCA is known to be a good approximation when alloying chemically similar elements with the same valence state. A detailed comparison of these two approaches is reported in IV B.

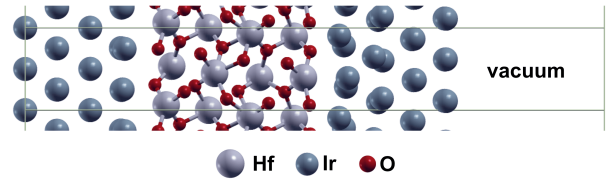


Figure 1. A sample simulation cell for a thin film relaxation of an Ir/ HfO_2 /Ir stack. HfO_2 is in the monoclinic phase with [001] orientation. The in-plane lattice is fixed to the lattice parameters of this phase and orientation of HfO_2 (see IV D for details of these thin film simulations). Periodic copies of the stack are separated by vacuum.

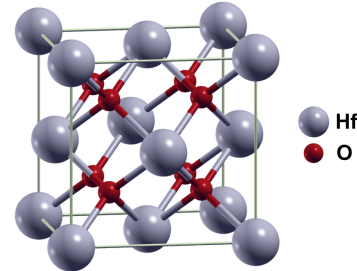


Figure 2. Cubic phase of HfO_2 (space group: $Fm\bar{3}m$), where hafnium atoms occupy the fcc lattice sites.

IV. RESULTS

A. Bulk phases of HfO_2

HfO_2 can be observed in three phases in its bulk form. The monoclinic phase (space group: $P2_1/c$) is stable all the way up to ~ 2000 K. Between ~ 2000 K and ~ 2900 K, the tetragonal phase (space group: $P4_2/nmc$) is observed. The highest symmetry cubic phase (space group: $Fm\bar{3}m$) is observed between ~ 2900 K and the melting temperature of ~ 3100 K [14, 15]. The cubic phase of HfO_2 is depicted in Figure 2. It is a face centered cubic structure with one formula unit per lattice point. The tetragonal and the monoclinic phases are obtained from the cubic phase through consecutive symmetry breaking operations.

These three bulk phases are all centrosymmetric, causing the bulk oxide to be paraelectric. However, as described in Section §III, the recent discovery of ferroelectricity in HfO_2 thin films indicates that a non-centrosymmetric orthorhombic phase (space group: $Pca2_1$) is stabilized under certain growth conditions that gives rise to a switchable polarization. The four phases of HfO_2 that are the focus of this study are shown in

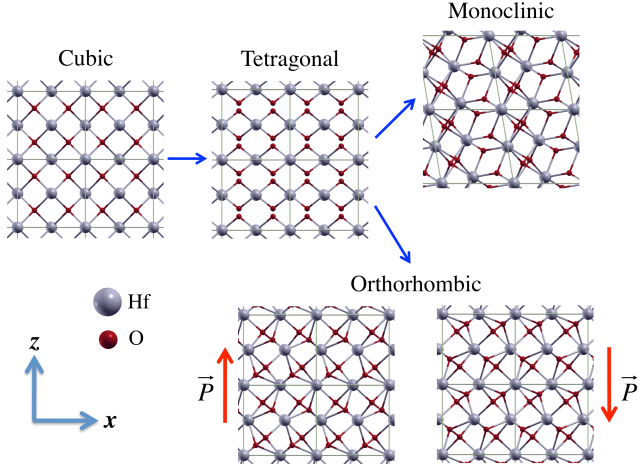


Figure 3. Bulk phases of HfO_2 considered in this work. Sub-group relations are shown by blue arrows. The cubic, tetragonal and monoclinic phases are the experimentally observed bulk phases. The non-centrosymmetric orthorhombic phase is observed in some thin films of HfO_2 and gives rise to ferroelectricity. For each phase, the 12-atom simulation cell that we use in this study is shown by thin straight lines.

Bulk phase	This work (GGA)	Ref. [38] (GGA)	Ref. [39] (LDA)	Ref. [40] (LDA)
mono $P2_1/c$	$\equiv 0.00$	$\equiv 0.00$	$\equiv 0.00$	$\equiv 0.00$
ortho $Pca2_1$	0.08	0.06	0.05	0.06
tetra $P4_2/nmc$	0.16	0.14	0.07	0.09
cubic $Fm\bar{3}m$	0.27	0.21	0.09	0.14

Table II. Energies of the bulk phases of HfO_2 in eV per HfO_2 (relative to the monoclinic phase) considered in this work, compared with previous computational work.

Figure 3. The orthorhombic and monoclinic phases are obtained from the tetragonal phase by symmetry breaking operations, indicated by a blue arrow in the figure.

In Table II we compare our computed energies of each phase (relative to the monoclinic phase) with the results from previous computational studies. We find that our results agree well with Ref. [38] which uses the GGA to approximate the exchange-correlation functional; and Refs. [39] and [40] which use the Local Density Approximation (LDA) agree with each other.

In Table III we compare lattice parameters with the

results of previous studies. We find that our results generally lie within the range of agreement among the previous works where there is a range of $<5\%$ for a given lattice parameter.

B. Effects of doping on bulk HfO_2

Due to its importance in the ferroelectric properties of hafnia thin films, we have investigated the role of doping in stabilizing the various phases of HfO_2 with respect to each other. We list the energies of bulk phases with respect to the monoclinic phase for various dopants in Table IV. These simulations are done with $2 \times 2 \times 2$ simulation cells with 96 atoms, where one Hf per cell (i.e., 1 in 32) is replaced by the dopant. All atomic positions and cell parameters are then relaxed. This leads to a doping ratio of 3.125% where the dopants are equally spaced in the three lattice directions. For elements with a different number of valence electrons than Hf, such as N, Al, Sr, Y and La, we have additionally computed relaxed energies with compensating electrons or holes and compared these with the neutral relaxations.

We find that doping does not change the energy difference between the orthorhombic and the monoclinic phases significantly. In some cases (C, N^* , Si and Ge), it reduces the energy of the tetragonal phase, while in some cases (C, N, N^* , Al^* , Si, Ge and Sr^*) it increases the energy of the cubic phase. We also find that changing the number of electrons in the cell does not significantly modify the energies of the orthorhombic and the tetragonal phases (with the exception of N), but increases the energy of the cubic phase (again with the exception of N). Our results are in close agreement with the available first-principles study of doped HfO_2 that included Ge, Sr, Y and La [42].

The most significant observation of this survey of dopants is that, for non-metal dopants (C, N^* , Si and Ge), the tetragonal phase experiences a significant stabilization. If we focus on the monoclinic, orthorhombic and tetragonal phases, which are the phases that participate in the thin film processes, we conclude that, apart from the cases of C, N^* , Si and Ge, no significant change occurs in terms of pure phase energetics. With these four special dopants, the reduction of energy in the tetragonal phase relative to the monoclinic phase may favor the formation of the tetragonal phase in thin films, and subsequently the formation of the ferroelectric orthorhombic phase during thermal annealing, as we will explain in IV C. To the best of our knowledge, C and N have not been used as dopants in HfO_2 ; thus it is not possible to refer to relevant experiments. Note that C and N have atomic radii much smaller than Hf, and hence are likely challenging to be incorporated as dopants. Ge and Ti have been reported as dopants in HfO_2 [43, 44]; however these reports were prior to the discovery of ferroelectric-

Bulk phase	Parameters	This work (\AA)	Ref. [38]	Ref. [41]	Ref. [40]
Monoclinic	$a, b, c,$ β	5.12, 5.18, 5.30, 99.6°	5.09, 5.16, 5.26, 99.7°	5.14, 5.20, 5.31, 99.8°	5.11, 5.18, 5.29, 99.7°
Orthorhombic	a, b, c	5.25, 5.04, 5.07	5.11, 4.90, 4.92	5.29, 5.01, 5.08	5.23, 5.04, 5.06
Tetragonal	a, c	5.07, 5.19	5.03, 5.15	5.06, 5.28	5.05, 5.14
Cubic	a	5.06	5.03	-	5.04

Table III. Lattice parameters (in \AA) of the bulk phases of HfO_2 compared with previous computational studies. For the monoclinic phase, β is the angle between \vec{a} and \vec{c} , which is the only non-perpendicular angle for this phase.

ity in hafnia-based films. The other elements we have included in our survey (Al, Sr, Y and La) have all been experimentally shown to promote ferroelectricity in hafnia [22, 27, 45]. Therefore, reduction of the energy of the tetragonal phase with respect to the monoclinic phase, by itself, does not predict the promotion of ferroelectricity in these films, and, it needs to be considered in conjunction with other factors such as strain and thin film effects.

1. Doping by Si

In order to gain a comprehensive understanding of the effects of doping by one of the elements, we focus on Si which is one of the most widely used dopants in hafnia-based thin films (along with Zr). In Figure 4, we present the environment of a hafnium atom by showing its bonds with the neighboring oxygen atoms for the (a) monoclinic, (b) orthorhombic, and (c) tetragonal phases of HfO_2 . We also present the environment of a silicon atom that replaces a hafnium atom after a full relaxation, for the (d) monoclinic, (e) orthorhombic, and (f) tetragonal phases.

As seen by the number of Hf-O bonds drawn in Figure 4, a hafnium atom is seven-fold coordinated by oxygen atoms in the monoclinic and orthorhombic phases and eight-fold coordinated in the tetragonal phase. A silicon dopant becomes five-fold coordinated in the monoclinic and orthorhombic phases and four-fold coordinated in the tetragonal phase. We list the (Hf,Si)-O distances in Table V. We assume that if the distance between the two atoms is not much larger than the sum of their atomic radii, the two atoms are coordinated. For Hf-O coordination, this sum is 2.2 \AA , and for Si-O coordination, it is 1.7 \AA , yielding the coordination numbers in Table V.

We find that the monoclinic and the orthorhombic phases have the same coordination configuration in HfO_2 , and the coordination of Si dopant is approximately the same for these two phases. Hence the energy difference between the orthorhombic and the monoclinic phases does not significantly change upon doping. However, in the tetragonal phase, the hafnium atom is coordinated

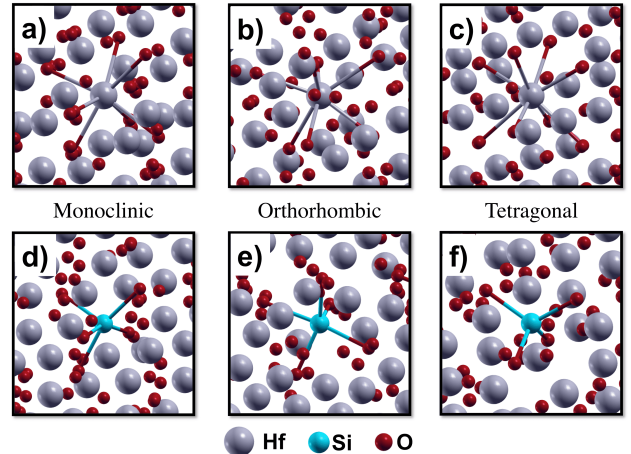


Figure 4. The environment of a Hf atom in the (a) monoclinic, (b) orthorhombic, and (c) tetragonal phases of HfO_2 compared with the environment of a substitutional Si dopant in the (d) monoclinic, (e) orthorhombic and (f) tetragonal phases. For each case, the bonds between the atom in question and its nearest oxygen neighbors are drawn. See Table V for the list of (Hf,Si)-O bond lengths in each case and the number of nearest oxygen neighbors (coordination number).

by 8 oxygens. A closer inspection reveals that Hf is surrounded by two concentric oxygen tetrahedra with Hf-O distances of 2.07 \AA and 2.39 \AA . After replacement of this hafnium with a silicon atom, the closer tetrahedron is pulled in and the farther tetrahedron is pushed out so that the distances become 1.69 \AA and 2.75 \AA . This oxygen environment for silicon is almost identical to its environment in the ground state of bulk SiO_2 . In the P3₁21 (α -quartz) phase of SiO_2 , silicon atoms lie in the centers of oxygen tetrahedra with a Si-O distance of 1.63 \AA (our calculated value). We note that among the low-energy polymorphs of SiO_2 , five out of six lowest energy structures feature tetrahedral cages [38]. Therefore, we conclude that the favorable tetrahedral environment of Si dopant in the tetragonal phase causes its significant stabilization with respect to the orthorhombic and the

Bulk phase	ortho Pca2 ₁	tetra P4 ₂ /nmc	cubic Fm $\bar{3}$ m
No doping	0.09	0.16	0.26
C	0.07	0.08	0.46
N	0.10	0.15	0.41
N* (-1e)	0.09	0.10	0.41
Al	0.09	0.16	0.28
Al* (+1e)	0.09	0.15	0.33
Si	0.07	0.11	0.33
Ti	0.09	0.15	0.27
Ge	0.09	0.12	0.30
Sr	0.08	0.16	0.23
Sr* (+2e)	0.10	0.18	0.34
Y	0.08	0.17	0.24
Y* (+1e)	0.09	0.17	0.29
La	0.08	0.16	0.24
La* (+1e)	0.08	0.16	0.29

Table IV. Energies of the bulk phases of HfO₂ in eV per HfO₂ (relative to the monoclinic P2₁/c phase) with 3.125% doping with various elements. The elements with a star (*) denote simulations with added electrons or holes to compensate for the difference in the number of valence electrons of that element and Hf. The number of extra electrons per simulation cell is shown next to each element in parentheses. For the case of N, one electron is taken out of the system, which is denoted as (-1e).

monoclinic phases. In the Supplementary Material, we list the dopant-O bond lengths for all the other dopants (C, N, N*, Al, Al*, Ti, Ge, Sr, Sr*, Y, Y*, La and La*).

We conclude the discussion on Si doping by comparing results obtained by atomic substitution (AS) to the virtual crystal approximation (VCA). In Table VI, we list the energies of the orthorhombic, tetragonal and cubic phases with respect to the monoclinic phase, for 2% and 4% Si-doped cases computed by VCA, and the 3.125% Si-doped case computed by AS and VCA. We find that VCA

Phase	Nearest O neighbor distances (Å)								C. N.
mono Hf	2.05	2.14	2.14	2.16	2.18	2.28	2.30		7
ortho Hf	2.04	2.12	2.13	2.14	2.14	2.24	2.27		7
tetra Hf	2.07	2.07	2.07	2.07	2.39	2.39	2.39	2.39	8
mono Si	1.76	1.79	1.80	1.83	1.87	2.36	2.92		5
ortho Si	1.75	1.77	1.81	1.81	1.92	2.27	3.07		5
tetra Si	1.69	1.69	1.69	1.69	2.75	2.75	2.75	2.75	4

Table V. List of (Hf,Si)-O bond lengths for each of the monoclinic, orthorhombic and tetragonal phases, for the undoped case (top three rows) and the 3.125% Si doped case. The number of oxygen neighbors to Hf or Si (coordination number) is reported in the rightmost column.

Phase	HfO ₂	2% Si (VCA)	3.125% Si (AS)	3.125% Si (VCA)	4% Si (VCA)
ortho	0.08	0.07	0.07	0.05	0.03
tetra	0.16	0.15	0.11	0.11	0.08
cubic	0.26	0.17	0.33	0.12	0.08

Table VI. Energies of the orthorhombic, tetragonal and cubic phases with respect to the monoclinic phase, for pure and Si doped HfO₂, as computed by direct atomic substitution (AS) for 3.125% and the virtual crystal approximation (VCA) for 2%, 3.125% and 4%. The energies are listed in eV per unit formula.

is in agreement with AS for the tetragonal phase, and gives an acceptable result for the orthorhombic phase. We have investigated the disagreement in the cubic phase by first inspecting the environment of the Si dopant in the case of AS. The eightfold coordination of hafnium persists for the silicon dopant. We have then relaxed the structure again after slightly displacing one of the neighboring oxygens, which has resulted in the transformation of the cell into a tetragonal cell, indicating that the cubic phase is unstable toward silicon doping. Hence, for the remainder of our study, we do not discuss the behavior of the cubic phase, which is also not observed in hafnia-based thin films.

	HfO ₂	$x = 0.75$	$x = 0.50$	$x = 0.25$	ZrO ₂
ortho (AS)	0.08	0.08	0.08	0.07	0.08
ortho (VCA)	0.08	0.07	0.07	0.07	0.08
tetra (AS)	0.16	0.14	0.14	0.14	0.12
tetra (VCA)	0.16	0.14	0.13	0.12	0.12
cubic (AS)	0.26	0.25	0.23	0.22	0.21
cubic (VCA)	0.26	0.20	0.19	0.19	0.21

Table VII. Energies of the orthorhombic, tetragonal and cubic phases with respect to the monoclinic phase, for $\text{Hf}_x\text{Zr}_{1-x}\text{O}_2$ where $x = 1.00, 0.75, 0.50, 0.25$ and 0.00 , as computed by atomic substitution (AS) and virtual crystal approximation (VCA). The energies are listed in eV per unit formula.

2. Hf/Zr mixing

Moving to the other most widely used dopant in hafnia thin films, we turn to Zr. In Table VII we list the energies of the orthorhombic, tetragonal and cubic phases with respect to the monoclinic phase for bulk $\text{Hf}_x\text{Zr}_{1-x}\text{O}_2$, where $x = 1.00, 0.75, 0.50, 0.25, 0.00$. For each case we compare the AS and the VCA results. For AS computations, we have used 4-unit-formula (12-atom) cells, and replaced 0 - 4 Hf atoms in the cell with Zr. For the 50% mixing case, where 2 Hf atoms per cell are substituted by Zr, we compute the energies for all possible 2-atom substitutions in the cell. These differently chosen pairs of atoms lead to relaxed energies within 0.02 eV of each other per unit formula, and the lowest such energy is reported for each phase.

We find that AS and VCA are in very good agreement for the orthorhombic and tetragonal phases, as in the Si-doped case. We could not determine the cause of the differences between these two methods for the cubic case, but since the cubic phase does not appear to participate in ferroelectricity of hafnia thin films, we have decided to leave this question for future research.

C. Effects of strain on doped HfO₂

1. Matching planes for bulk phases

It has been observed that ferroelectric hafnia thin films have large numbers of tetragonal grains in the early stages of growth [11, 12, 30, 31]. This is understood to be caused by a reduction of the relative energy of the

tetragonal phase through its low surface energy [29, 46] and enhanced by doping. We have shown that for 3 - 4% Si doping, the tetragonal phase is significantly stabilized which agrees with previous computational studies [47, 48]. We have also shown that for Zr mixing above 25%, the tetragonal phase is also stabilized, again in agreement with prior works [40, 48]. In IV D, we will confirm that the interface energy of the tetragonal phase with a common metal electrode is indeed competitive with the other phases. Hence it is reasonable to think that a significant fraction of the initial grains during film growth are tetragonal. Our hypothesis is that, after the deposition of the top electrode and during thermal annealing, some portion of these tetragonal grains transform into orthorhombic grains. We now investigate this scenario in more detail and show that it is plausible for certain doping ranges. Our main physical assumption will be that during the potential transformation of a tetragonal grain into other phases, the grain is geometrically *confined* within the film by the surrounding grains: that it cannot change its in-plane area significantly during the transformation.

In order for an out-of-plane polarized ([001] oriented) orthorhombic grain to form without a large change in the in-plane lattice parameters, the parent tetragonal grain needs to have the orientation [100] or [010] (which are physically equivalent). We demonstrate these matchings pictorially in Figure 5. The short sides of the tetragonal phase (a_t) and the orthorhombic phase (b_o, c_o) are similar in length; and the long sides of these two phases (c_t and a_o) are also similar in length (see Table III for computed values). Therefore the tetragonal cell can transform into the orthorhombic cell by slightly elongating c_t and slightly contracting one of the a_t .

Repeating the same analysis for the monoclinic phase, we eliminate the m[001] \longleftrightarrow o[001] transformation because of the mismatch in lengths, and the m[010] \longleftrightarrow o[001] transformation because of the mismatch in the angles between the in-plane lattice vectors. Therefore the constrained-area transformations that can lead to a [001] oriented orthorhombic phase are:

$$\text{m}[100] \longleftrightarrow \text{t}[100] \longleftrightarrow \text{o}[001].$$

2. Effects of strain on undoped grains

To investigate the likelihood of the tetra \rightarrow mono and the tetra \rightarrow ortho transformations, we have simulated epitaxially strained phases of hafnia via computational relaxations of bulk hafnia strained to pre-specified lattice parameters. For each of the three phases, we have applied -4%, -2%, 0%, 2% and 4% biaxial strain to each of the in-plane lattice parameters with respect to their unstrained values, and relaxed the third lattice parameter as well as all the atomic positions. In Figure 6, we plot the

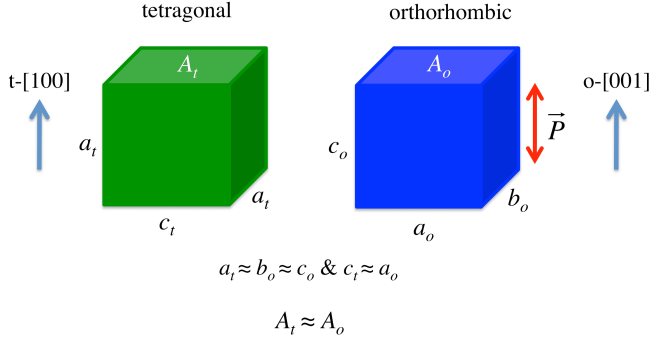


Figure 5. Conventional unit cells of the tetragonal and the orthorhombic phases, and the approximate equalities between their lattice parameters and lattice planes. The polarization vector lies in the $[001]$ direction of the orthorhombic phase. A $[100]$ -oriented tetragonal grain can transform into a $[001]$ -oriented out-of-plane polarized orthorhombic grain by a set of small changes in the lattice parameters. The quantities A_t and A_o refer to the constrained planar areas of the two phases.

energies of the three phases of HfO_2 versus the area of the matching plane. For each phase, we fit a third degree polynomial to the five data points we have obtained to generate a smooth curve.

A $t[100]$ grain with energy-optimal in-plane area may transform into the orthorhombic and the monoclinic phases without changing its area, which would be represented in Figure 6 as a downward jump from the bottom of the green curve to a point on either the blue or the black curve. Because at the optimized area of the $t[100]$ grain the monoclinic phase is 0.18 eV lower than the orthorhombic phase, the likelihood of the tetra \rightarrow mono transformation should be much higher than the likelihood of the tetra \rightarrow ortho transformation. We also circle in Figure 6 the point at which the curves that correspond to the monoclinic and the orthorhombic phases cross. That point corresponds to a 3% compressive biaxial strain with respect to the $t[100]$ grain. Therefore, in the absence of a mechanism that generates such a compressive strain, the grain is expected to transform into a $m[100]$ grain during annealing.

To promote the transformation to the $o[001]$ instead, Batra *et al.* introduced an electric field [49] and showed that the orthogonal phase can be made favorable with the application of fields that are experimentally feasible. Below, we explore the effects of a different physical factor, the dopant kind and density, on the energy versus area curves in Figure 6.

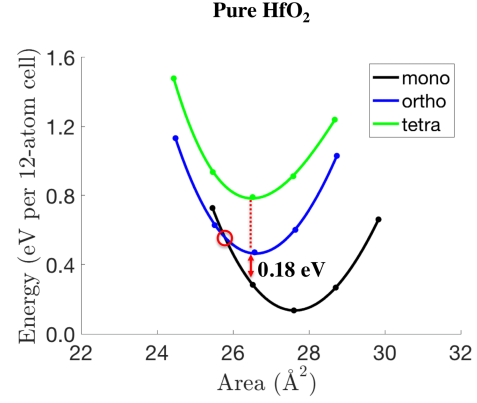


Figure 6. Energies of the monoclinic, orthorhombic and tetragonal phases vs. in-plane matching area for epitaxially strained bulk simulations of pure HfO_2 . For each phase, five data points at -4%, -2%, 0%, 2% and 4% in-plane strain are simulated (circular marks). The curves are obtained by fitting cubic polynomials to these five data points. The energy difference between the orthorhombic and the monoclinic phases at the optimized area of the $t[100]$ grain is equal to 0.18 eV per 12-atom cell, and labelled in the figure. The zero of energy is chosen arbitrarily.

3. Effects of strain on Si:HfO₂

We repeat the same set of simulations for the 2% and the 4% Si doped HfO_2 as modeled by the VCA. We present the results in Figure 7.

We observe in Figure 7 (a) that for the 2% Si doped HfO_2 , the energy difference between the orthorhombic and the monoclinic phases at the optimized area of $t[100]$ grains is 0.09 eV, which is lower than the undoped value of 0.18 eV. The mono/ortho crossing occurs at 1% compressive strain as opposed to 3% in the undoped case. Hence the formation of the $o[001]$ grains through the $t[100]$ grains is favored by Si doping. In the case of 4% Si doping shown in Figure 7 (b), the mono/ortho crossing occurs at zero strain relative to the optimal tetragonal in-plane area. Thus from a purely energetic point of view, an optimized $t[100]$ grain has equal chance of transforming into an $o[001]$ grain or an $m[100]$ grain.

In Table VIII we summarize our findings on the epitaxially strained Si-doped HfO_2 . As the doping concentration increases, the energy difference between the orthorhombic and the monoclinic phases at the optimized in-plane area of $t[100]$ grains decreases. At 4% doping, the energies of the $o[001]$ and $m[100]$ grains coincide for the in-plane area that is optimized for $t[100]$ grains. However, the tetra \rightarrow mono transformation that keeps the area fixed increases the volume of the cell by 5%, whereas the tetra \rightarrow ortho transformation that keeps the area fixed decreases the volume by 1%. Therefore, in

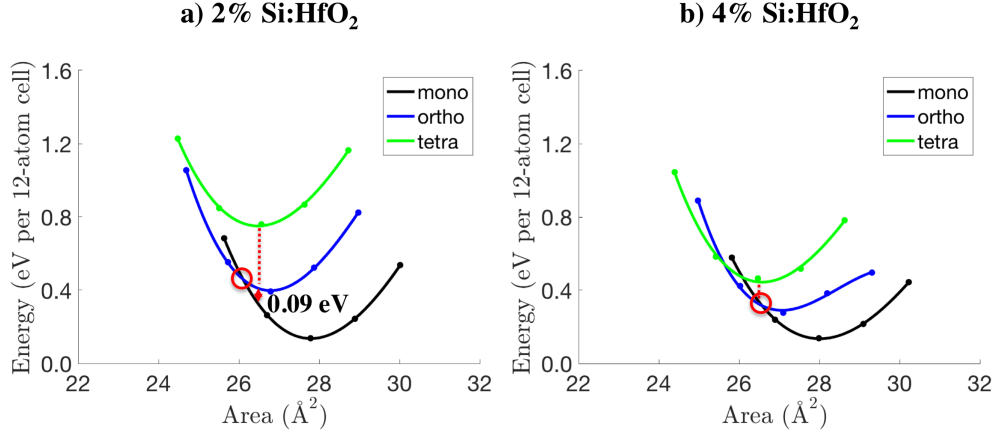


Figure 7. Energies of the monoclinic, orthorhombic and tetragonal phases vs in-plane matching area for epitaxially strained bulk simulations of (a) 2% Si doped and (b) 4% Si doped HfO_2 . For each composition and phase, five data points at -4%, -2%, 0%, 2% and 4% in-plane strain are simulated (circular marks). The curves are obtained by fitting cubic polynomials to these five data points. The energy difference between the orthorhombic and the monoclinic phases at the optimized area of the t [100] grain is labelled in the figure in (a), and is equal to zero in (b). The zero of energy is chosen arbitrarily.

	HfO_2	2% Si	4% Si
% strain where $E(o) = E(m)$	-1.3%	-0.7%	0.2%
$E(t) - E(o)$ (eV)	0.32	0.34	0.12
$E(t) - E(m)$ (eV)	0.50	0.43	0.12

Table VIII. Key numerical results described in Figures 6 and 7. The strain values reported are biaxial strain with respect to the optimized in-plane area of the [100] oriented tetragonal phase when the energies of the orthorhombic and the monoclinic phases coincide. The energy differences are taken at the optimized in-plane area of the [100] oriented tetragonal phase and reported in eV per 12-atom cell.

the presence of a top electrode that provides additional out-of-plane confinement, the tetra \rightarrow ortho transformation may have a further advantage compared to the tetra \rightarrow mono transformation. Our findings offer an explanation for the experimental observation that 3-4% Si doped films that are subjected to high temperature annealing with a top electrode have ferroelectric properties; i.e., >2% doping (in the case of silicon) and pre-annealing deposition of the top electrode are necessary conditions for ferroelectricity (see Section §II).

4. Effects of strain on $\text{Hf}_x\text{Zr}_{1-x}\text{O}_2$

As one of the most common hafnia derivatives that has successfully been used as a ferroelectric thin film, we re-

peat the above analysis of strain effects for $\text{Hf}_x\text{Zr}_{1-x}\text{O}_2$. We present our results in Figure 8. We find that the energy difference between the orthorhombic and the monoclinic phases at the optimized area of t [100] grains is (a) 0.14 eV for $x = 0.75$, (b) 0.04 eV for $x = 0.50$, (c) 0.13 eV for $x = 0.25$ and (d) 0.18 eV for pure ZrO_2 (per 12-atom cell). Hence HfZrO_4 ($x = 1/2$) presents the most suitable situation for the tetra \rightarrow ortho transformation.

In Table IX we report our relevant results for $\text{Hf}_x\text{Zr}_{1-x}\text{O}_2$. The energy difference between the orthorhombic and the monoclinic phases at the optimized in-plane area of t [100] grains is minimized at $x = 0.50$. For this case, the energies of the o [001] and m [100] grains coincide for the in-plane area that is 1% compressively strained with respect to the optimized area for t [100] grains. Without the strain, the tetra \rightarrow mono transformation is preferred to the tetra \rightarrow ortho transformation by 0.04 eV per 12-atom cell. However, the former increases the volume by 3%, whereas the latter increases the volume by 1%. Therefore the confinement effects provided by the top electrode may favor the tetra \rightarrow ortho transformation over the tetra \rightarrow mono transformation. As in the case of Si doping, our findings explain the experimental observation that 30 - 60% Zr doped films that are annealed with a capping electrode present ferroelectric properties (see Section §II).

In addition, we observe that for $\text{Hf}_{0.25}\text{Zr}_{0.75}\text{O}_2$ and ZrO_2 , the energy versus strain curves that represent the tetragonal and the orthorhombic phases lie closer to each other (see Figure 8). In Table IX, we notice that the energy difference between the optimized t [100] grains and the o [100] grains with the same area is lowest for high Zr:Hf ratios. Because the orthorhombic $\text{Pca}2_1$ space group is a subgroup of the tetragonal $\text{P}4_2/\text{nmc}$ space

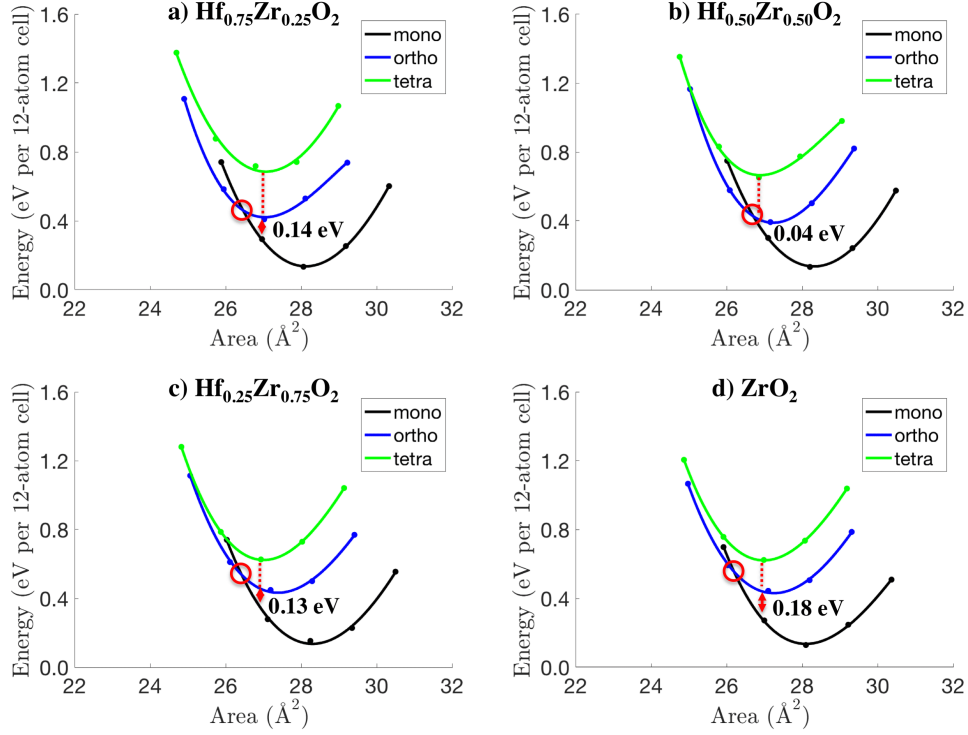


Figure 8. Energies of the monoclinic, orthorhombic and tetragonal phases vs in-plane matching area for epitaxially strained bulk simulations of (a) $\text{Hf}_{0.75}\text{Zr}_{0.25}\text{O}_2$, (b) $\text{Hf}_{0.50}\text{Zr}_{0.50}\text{O}_2$, (c) $\text{Hf}_{0.25}\text{Zr}_{0.75}\text{O}_2$ and (d) pure ZrO_2 . For each composition and phase, five data points at -4%, -2%, 0%, 2% and 4% in-plane strain are simulated (circular marks). The curves are obtained by fitting cubic polynomials to these five data points. The energy difference between the orthorhombic and the monoclinic phases at the optimized area of the t [100] grain is labelled in the figure in for each case. The zero of energy is chosen arbitrarily.

	HfO ₂	$x = 0.75$	$x = 0.50$	$x = 0.25$	ZrO ₂
% strain where $E(o) = E(m)$	-1.3%	-1.0%	-0.4%	-1.0%	-1.5%
$E(t) - E(o)$ (eV)	0.32	0.27	0.26	0.17	0.18
$E(t) - E(m)$ (eV)	0.50	0.43	0.30	0.30	0.36

Table IX. Key numerical results described in Figures 6 and 8 for $\text{Hf}_x\text{Zr}_{1-x}\text{O}_2$ where $x = 1.00, 0.75, 0.50, 0.25$ and 0.00 . The strain values reported are biaxial strain with respect to the optimized in-plane area of the [100] oriented tetragonal phase when the energies of the orthorhombic and the monoclinic phases coincide. The energy differences are taken at the optimized in-plane area of the [100] oriented tetragonal phase, and reported in eV per 12-atom cell.

group, the proximity in their energies promotes antiferroelectricity [39]. This supports the experimental observation of antiferroelectric behavior in thin films with

higher Zr content (see Section §III).

5. Effects of strain on (Al, Ge, Ti, La):HfO₂

To conclude this section, we repeat the strain analysis for four additional dopants: Al, Ge, Ti and La. Our results are summarized in Table X, and the energy versus in-plane matching area plots are in the Supplementary Material.

We observe that the effect of strain on the Al-doped bulk HfO_2 is very similar to that on the Si-doped bulk HfO_2 . The strain values at which the energies of the orthorhombic and the monoclinic phases coincide for these two dopants at 4% doping are close to zero (0.2% for Si and 0.3% for Al); therefore, the transformation from the tetragonal phase to the orthorhombic phase during annealing is expected to be robust for both dopants. This is in agreement with experiments which have found that the ferroelectric properties of Si- and Al-doped HfO_2 are similar [22, 27].

We also observe that the 2% and 4% doping percentages for Ge, Ti and La do not improve on the required strain values for the crossing of energies of the orthorhombic and the monoclinic phases compared to undoped

HfO₂. Therefore, we predict that Ge and Ti may not perform as well as Si and Al as dopants in HfO₂ in terms of promoting ferroelectricity at low doping concentrations even though their atomic radii are very close to those of Si and Al. Our similar prediction regarding La is at odds with experiments to date in which La:HfO₂ has yielded high P_r values [22, 45]. However, in these experiments, the doping concentration was greater than 5%, which is beyond the reliable range of our VCA method for non-isovalent elements. We leave a detailed analysis of the case of La for future research.

Our analysis in this section supports our hypothesis that some of the initially formed tetragonal grains transform into out-of-plane polarized orthorhombic grains during thermal annealing. This requires these grains to be confined in-plane by the surrounding grains, and out-of-plane by the bottom and top electrodes. The ideal doping range for this transformation is $\sim 4\%$ for Si and Al, and $\sim 50\%$ for Zr.

D. Thin film simulations

In addition to the combined effects of doping and strain, we have performed investigations on interface effects. In hafnia-based thin films, ferroelectricity occurs when the film is ~ 8 -24 nm thick, and the grains are generally a few nm in size. This makes finite-size effects potentially important. Surfaces of ZrO₂ and HfO₂ have been studied experimentally [50, 51] and theoretically [29, 52–54] prior to the discovery of ferroelectricity in these films, with a focus on the monoclinic and tetragonal phases. A recent study has included the polar orthorhombic Pca2₁ phase into a first principles investigation of surfaces of hafnia [46].

Our goal is to compute the energies of the interfaces between relevant phases of hafnia and typical electrodes such as TiN and Ir. In Figure 9, we schematically depict an Ir/HfO₂/Ir stack. In order to isolate thin film effects from strain effects, we fix the in-plane lattice parameters to the lattice parameters of the HfO₂ phase in the orientation that we choose to study. We have found that the lattice parameters of HfO₂ are in the range of 5.04-5.30 Å (see Table III). On the other hand, typical electrodes used with hafnia thin films, e.g. TiN and Ir, have lattice constants of 4.24 Å and 3.90 Å, respectively. To faithfully use these electrode lattice constants, we would need to simulate very large supercells to create heterostructures where no significant strain occurs on either the metal or the oxide. However, we believe that such a calculation is not needed as a first pass, since epitaxial growth is not actually observed in the experimental systems. Therefore, we study the interfaces using much more reasonably sized $\sqrt{2} \times \sqrt{2}$ cells of Ir ($a = 5.52$ Å) with HfO₂, where the Ir is strained to match various phases and orientations of HfO₂. A similar TiN cell would have a lattice

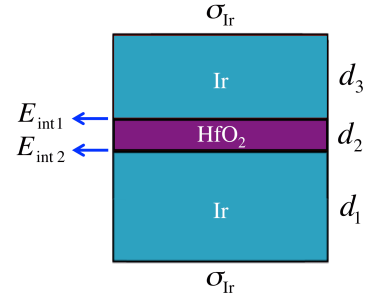


Figure 9. Schematic demonstration of a Ir/HfO₂/Ir stack simulation. d_1 , d_2 and d_3 denote the thicknesses of the components of the stack, σ_{Ir} denotes the surface energy of Ir, and $E_{\text{int } 1}$ and $E_{\text{int } 2}$ denote interface energies of the two Ir/HfO₂ interfaces.

constant of 6.00 Å and thus require a huge compressive strain, so we drop TiN from this initial study and focus on Ir. Lastly, we emphasize that these are *model* calculations: the theoretical simulation has periodic boundary conditions and thus is always epitaxial while the experimental interfacial structure is much more complex, non-epitaxial, and unknown with any precision at present. Moreover, in our calculations, the Ir layers are significantly strained, and thus they represent only an idealized model representation of a metal electrode rather than the actual material used in the experiment. Our aim is to use a first-principles approach to the interfacial energetics to gauge their *approximate* size and *possible* importance under the assumption that the interaction of HfO₂ with this theoretical model electrode is a good proxy to the actual interfacial interaction. Although Ir is employed less frequently than TiN in the experiments, it fits better into our approach because it undergoes small relaxations when interfaced with HfO₂. In contrast, our trial simulations of TiN/HfO₂ interfaces exhibited large distortions and formed cross-interface chemical bonds between Ti and O atoms.

In order to compute the interfacial energies in a stack as shown in Figure 9, we first define the surface energy of the free-standing Ir thin film as

$$2\sigma_{\text{Ir}} = E_{\text{film}}^{(\text{Ir})}(d) - d \times E_{\text{bulk}}^{(\text{Ir})}, \quad (1)$$

where $E_{\text{film}}^{(\text{Ir})}(d)$ is the computed energy of the free-standing strained Ir film, $E_{\text{bulk}}^{(\text{Ir})}$ is the energy per u.c. of the bulk strained Ir, and d is the thickness of the Ir film in units of unit cells. An accurate way to extract σ_{Ir} is to compute $E_{\text{film}}^{(\text{Ir})}(d)$ as a function of d and fit a straight line, treating σ_{Ir} and $E_{\text{bulk}}^{(\text{Ir})}$ as fitting parameters [55]. For this task, we have used $d = 2, 3, 4, 5, 6$ u.c. (each unit cell of Ir consists of two atomic layers). The resulting surface energies are listed in Table XI.

	HfO ₂	2% Al	4% Al	2% Ge	4% Ge	2% Ti	4% Ti	2% La	4% La
% strain where $E(o) = E(m)$	-1.3%	-0.4%	0.3%	-1.6%	-2.0%	-1.3%	-1.6%	-1.5%	-1.4%
$E(t) - E(o)$ (eV)	0.32	0.29	0.07	0.32	0.34	0.28	0.29	0.31	0.30
$E(t) - E(m)$ (eV)	0.50	0.35	0.07	0.58	0.65	0.44	0.52	0.51	0.50

Table X. Summary of the energy vs. strain results for (Al, Ge, Ti, La):HfO₂. The strain values reported are biaxial strain with respect to the optimized in-plane area of the [100] oriented tetragonal phase when the energies of the orthorhombic and the monoclinic phases coincide. The energy differences are taken at the optimized in-plane area of the [100] oriented tetragonal phase, and reported in eV per 12-atom cell. Energy vs. in-plane matching area curves for these four dopants and two doping percentages are presented in the Supplementary Material.

Once we have found σ_{Ir} for a given phase and orientation of HfO₂, we calculate the interfacial energies E_{int} as

$$E_{\text{int } 1} + E_{\text{int } 2} = E_{\text{stack}} - (d_1 + d_3) E_{\text{bulk}}^{(\text{Ir})} - d_2 E_{\text{bulk}}^{(\text{HfO}_2)} - 2\sigma_{\text{Ir}}, \quad (2)$$

where E_{stack} is the computed energy of the final materials stack, $E_{\text{bulk}}^{(\text{Ir})}$ is the energy per u.c. of the bulk strained Ir, $E_{\text{bulk}}^{(\text{HfO}_2)}$ is the energy per u.c. of bulk HfO₂, and the thicknesses d_1 , d_2 and d_3 are shown in Figure 9 and are in unit cells. We note that we can only compute the sum of the two interfacial energies using this approach; if the interfaces are physically identical, then a single interface energy becomes available.

The relaxed configuration of the Ir/HfO₂/Ir stack with $d_1 = d_2 = d_3 = 2$ u.c. where HfO₂ is in the monoclinic-[001] configuration is shown in Figure 1. To find the lowest energy interfaces for a given phase and orientation, we have first simulated possible surface terminations of HfO₂. In order to include an integer number of unit cells in the thin film (i.e., stoichiometric hafnia), we have restricted the terminations to be Hf on one end and O on the other (Hf-...-OO) or O terminated on both ends (O-...-O). Prior work on zirconia has shown that the energy of an O-...-O terminated slab is lower in energy than a Zr-...-OO terminated slab by 13.0 eV per in-plane cell for t[001] films of free-standing ZrO₂ [56]. Analogous results have been reported for hafnia as well [46]. We have found a very similar (and huge) value of 13.4 eV for free-standing HfO₂ by simulating 2 u.c. thick t[001] films. To check that the Hf-...-OO termination remains high-energy for oxide/metal interfaces, we have simulated HfO₂/Ir stacks with the cubic phase for (Ir)-Hf-...-OO-(Ir), (Ir)-OO-...-Hf-(Ir) and (Ir)-O-...-O-(Ir) terminations. We have found that the (Ir)-Hf-...-OO-(Ir) and (Ir)-OO-...-Hf-(Ir) stacks are 6.3 and 7.8 eV per in-plane cell higher in energy than the (Ir)-O-...-O-(Ir) stack, respectively. Therefore, we have decided to restrict our studies to the O-...-O terminated HfO₂ films for all phases of hafnia. In order to find the lowest energy interface for each HfO₂ phase and orientation, we have

	$2\sigma_{\text{Ir}}$ (eV)	$E_{\text{int } 1} + E_{\text{int } 2}$ (eV)
monoclinic-[001]	8.8	5.7
monoclinic-[100]	9.5	9.8
orthorhombic-[001]	8.6	7.4
orthorhombic-[100]	7.7	7.0
orthorhombic-[010]	8.8	13.4
tetragonal-[001]	7.8	13.3
tetragonal-[100]	8.6	6.9
cubic-[001]	7.8	11.4

Table XI. Surface energies for strained iridium slabs and interface energies for Ir/HfO₂/Ir stacks for each HfO₂ phase and orientation computed via equation (1) and equation (2), respectively. Energies are listed in eV per in-plane cell.

run relaxations for the top and bottom interfaces separately, using a 2×2 lateral grid of initial HfO₂ positions relative to Ir for each case. After finding the optimal coordinates for the top and bottom interfaces separately, we have joined them to make the Ir/HfO₂/Ir stacks, and then fully relaxed the atomic positions (except for the surface u.c. of Ir).

We have studied the interfaces of Ir and pure HfO₂ in the monoclinic, tetragonal, orthorhombic and cubic phases, in all possible inequivalent principle orientations. The only exception is the m[010] orientation, which is excluded because of the non-orthogonal in-plane lattice vectors. To extract $E_{\text{int } 1} + E_{\text{int } 2}$ accurately from equation (2), we have computed $E_{\text{stack}}(d_1, d_2, d_3)$ with $d_1 = d_3 = 2, 3, 4$ u.c. and $d_2 = 2, 3, 4$ u.c., fitting a linear equa-

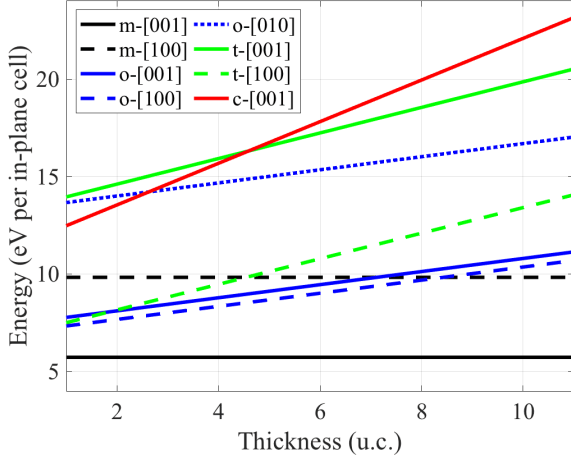


Figure 10. Thin film energies computed via the model described in equation (3) as a function of film thickness for Ir/HfO₂/Ir stacks. The zero of the bulk energies is taken as the monoclinic phase, causing the lines corresponding to this phase (black) to be flat. The orthorhombic, tetragonal and cubic phases are represented by blue, green and red lines, respectively.

tion with $E_{\text{bulk}}^{(\text{Ir})}$, $E_{\text{bulk}}^{(\text{HfO}_2)}$ and $E_{\text{int } 1} + E_{\text{int } 2} + 2\sigma_{\text{Ir}}$ as the fitting parameters. After extracting $E_{\text{int } 1} + E_{\text{int } 2} + 2\sigma_{\text{Ir}}$, we have used the σ_{Ir} values found earlier to compute $E_{\text{int } 1} + E_{\text{int } 2}$ for each case. We have found that all phases and orientations are mechanically stable in thin film form, with modest relaxations at both Ir/HfO₂ interfaces. We list the interface energies we have found in Table XI. Our results are in the range of 5-13 eV, which is comparable to the 4-12 eV range found for (twice) the surface energies of HfO₂ [46].

With the interface energies we have obtained via equation (2) and listed in Table XI, we build an energetic model for variable-thickness films based on our interfacial energies and bulk hafnia energies using the formula:

$$E_{\text{film}}^{(\text{ph-or})}(d) = E_{\text{int } 1}^{(\text{ph-or})} + E_{\text{int } 2}^{(\text{ph-or})} + dE_{\text{bulk}}^{(\text{ph})}, \quad (3)$$

where $E_{\text{film}}^{(\text{ph-or})}(d)$ is the energy of the thin film of HfO₂ in a given phase and orientation “ph-or”, d is the thickness of the hafnia in u.c., and $E_{\text{bulk}}^{(\text{ph})}$ is the energy of one unit cell of HfO₂ in phase “ph”.

We summarize the results of this model in Figure 10 as a plot of energy vs. thickness for each of the phase-orientation pairs we have studied. We define $E_{\text{bulk}}^{(\text{mono})}$ to be zero, so the lines that correspond to the monoclinic phase are horizontal. We observe that, because of variations in the interface energies that are of the order of a few eV per in-plane cell, several crossings occur. Even though the m[001] grains remain as the lowest energy configuration for all thicknesses, we find that for

ultra-thin films, o[001], o[100] and t[100] grains are also competitive (see also Table XI for the interface energy values). If some t[100] grains are formed initially, they may become kinetically trapped as the film grows further. The energy of the t[100] film crosses the energies of the o[001] films approximately at a thickness of 2 unit cells. For thicker films, o[001] grains are more favorable than t[100] grains, but less favorable than m[100]. Hence, this simple model predicts that t[100] grains may initially form during growth and then transform into o[001], o[100], m[001] or m[100] grains during annealing. The matching plane arguments from IV C disfavor the transformation into o[100], m[001]; hence we would expect t[100] → m[100] and t[100] → o[001] transformations to dominate. Our thin film results thus agree with the t[100] → (m[100], o[001]) picture above; however, the doping-induced modifications in the energy vs. strain curves, presented in IV C, as well as volumetric confinement, are necessary to favor the t[100] → o[001] transformation over the t[100] → m[100] transformation. In summary, our interfacial model indicates that interface effects (1) are *significant* and can *dominate* in the early stages of growth, and (2) do not explain the observed properties of the films unless they are considered *in conjunction* with doping and strain effects. We expect these overall conclusions to be true for all electrodes employed in the experiments including TiN.

Our model has a number of limitations. Two that can be addressed relatively easily in future studies are: (1) The simulation for every phase and orientation is done at the unstrained lattice parameters of that phase and orientation. The electrode is assumed to be unaffected by strain in any significant way. This assumption can be tested by applying small strain to each phase and orientation and re-computing the interface energies to check that they do not change in irregular ways. (2) The films are assumed to stay exactly stoichiometric, i.e. an exact monolayer (ML) of oxygen (and then a ML of hafnium) at both interfaces. Further simulations can be run with 0, 0.5, 1.5 and 2 ML of oxygen at the interfaces, yielding differing energy vs. thickness lines in Figure 10.

V. CONCLUSION

We have conducted a first-principles study of doped hafnia with the goal of understanding some of the experimental observations concerning ferroelectricity from a structural point of view. We have described the effects of various dopants on the energetics of bulk phases of HfO₂. We have discussed in detail the structural changes that are caused by Si doping. We have compared two computational methods for modeling doping: atomic substitution (AS) and the virtual crystal approximation (VCA). We have found that VCA compares well with AS and used VCA to simulate the effects of epitax-

ial strain on doped HfO_2 . We have found that among 0%, 2% and 4% Si doping, 4% doping provides the best conditions for initial tetragonal [100] grains to transform into orthorhombic [001] grains. We have also found that for $\text{Hf}_x\text{Zr}_{1-x}\text{O}_2$, $x = 0.5$ provides the most favorable conditions for the tetragonal [100] \rightarrow orthorhombic [001] transformation. However, for this transformation to be preferred over the tetragonal [100] \rightarrow monoclinic [100] transformation, some confinement needs to be present. In experiments, this confinement is provided by a top electrode (typically TiN). Our findings provide an explanation for common experimental observations for the optimal ranges of doping in Si:HfO_2 and $\text{Hf}_x\text{Zr}_{1-x}\text{O}_2$. Repeating the same analysis for Al, Ti, Ge and La, we have found that Al: HfO_2 behaves similarly to Si:HfO_2 ; whereas Ti, Ge or La doping only slightly modifies the strain response of pure HfO_2 . Finally, we have described a model to estimate the interface effects for thin films of hafnia, based on *ab initio* simulations of Ir/ HfO_2 /Ir stacks. Our results offer interesting clues for how the interface effects may be in play for the stabilization of the ferroelectric phase in these films.

VI. ACKNOWLEDGEMENTS

This work was supported by the National Science Foundation under Award 1609162 and by the grant MR-SEC DMR-1119826. We thank the Yale Center for Research Computing for guidance and use of the research computing infrastructure, with special thanks to Stephen Weston and Andrew Sherman. Additional computational support was provided by NSF XSEDE resources via Grant TG-MCA08X007.

-
- [1] R. A. McKee, F. J. Walker, and M. F. Chisholm, *Science* **293**, 468 (2001), ISSN 0036-8075, 1095-9203, URL <http://www.sciencemag.org/content/293/5529/468>.
 - [2] J. Hoffman, X. Pan, J. W. Reiner, F. J. Walker, J. P. Han, C. H. Ahn, and T. P. Ma, *Advanced Materials* **22**, 2957 (2010), ISSN 1521-4095, URL <http://onlinelibrary.wiley.com/doi/10.1002/adma.200904327/abstract>.
 - [3] D. P. Kumah, M. Dogan, J. H. Ngai, D. Qiu, Z. Zhang, D. Su, E. D. Specht, S. Ismail-Beigi, C. H. Ahn, and F. J. Walker, *Physical Review Letters* **116**, 106101 (2016), URL <http://link.aps.org/doi/10.1103/PhysRevLett.116.106101>.
 - [4] M. Dogan, S. Fernandez-Peña, L. Kornblum, Y. Jia, D. P. Kumah, J. W. Reiner, Z. Krivokapic, A. M. Kolpak, S. Ismail-Beigi, C. H. Ahn, et al., *Nano Letters* **18**, 241 (2018), ISSN 1530-6984, URL <http://dx.doi.org/10.1021/acs.nanolett.7b03988>.
 - [5] T. P. Ma and J.-P. Han, *IEEE Electron Device Letters* **23**, 386 (2002), ISSN 0741-3106.
 - [6] S. Dünkel, M. Trentzsch, R. Richter, P. Moll, C. Fuchs, O. Gehring, M. Majer, S. Wittek, B. Müller, T. Melde, et al., in *2017 IEEE International Electron Devices Meeting (IEDM)* (2017), pp. 19.7.1–19.7.4.
 - [7] N. Gong and T. Ma, *IEEE Electron Device Letters* **37**, 1123 (2016), ISSN 0741-3106.
 - [8] Y.-K. Chiou, C.-H. Chang, and T.-B. Wu, *Journal of Materials Research* **22**, 1899 (2007), ISSN 2044-5326, 0884-2914, URL <https://doi.org/10.1557/jmr.2007.0242>.
 - [9] M. H. Park, Y. H. Lee, H. J. Kim, Y. J. Kim, T. Moon, K. D. Kim, J. Müller, A. Kersch, U. Schroeder, T. Mikolajick, et al., *Advanced Materials* **27**, 1811 (2015), ISSN 1521-4095, URL <http://onlinelibrary.wiley.com/doi/10.1002/adma.201404531/abstract>.
 - [10] G. D. Wilk, R. M. Wallace, and J. M. Anthony, *Journal of Applied Physics* **89**, 5243 (2001), ISSN 00218979, URL http://jap.aip.org/resource/1/japiau/v89/i10/p5243_s1.
 - [11] T. Boscke, J. Müller, D. Brauhaus, U. Schroder, and U. Böttger, in *Electron Devices Meeting (IEDM), 2011 IEEE International* (2011), pp. 24.5.1–24.5.4.
 - [12] J. Müller, T. S. Böske, U. Schröder, S. Mueller, D. Bräuhaus, U. Böttger, L. Frey, and T. Mikolajick, *Nano Letters* **12**, 4318 (2012), ISSN 1530-6984, URL <http://dx.doi.org/10.1021/nl302049k>.
 - [13] N. Gong, X. Sun, H. Jiang, K. S. Chang-Liao, Q. Xia, and T. P. Ma, *Applied Physics Letters* **112**, 262903 (2018), ISSN 0003-6951, URL <https://aip.scitation.org/doi/10.1063/1.5010207>.
 - [14] J. Wang, H. P. Li, and R. Stevens, *Journal of Materials Science* **27**, 5397 (1992), ISSN 0022-2461, 1573-4803, URL <http://link.springer.com/article/10.1007/BF00541601>.
 - [15] X. Zhao and D. Vanderbilt, *Physical Review B* **65**, 233106 (2002), URL <http://link.aps.org/doi/10.1103/PhysRevB.65.233106>.
 - [16] J. Müller, U. Schröder, T. S. Böske, I. Müller, U. Böttger, L. Wilde, J. Sundqvist, M. Lemberger, P. Kücher, T. Mikolajick, et al., *Journal of Applied Physics* **110**, 114113 (2011), ISSN 0021-8979, 1089-7550, URL <http://scitation.aip.org/content/aip/journal/jap/110/11/10.1063/1.3667205>.
 - [17] S. Mueller, J. Mueller, A. Singh, S. Riedel, J. Sundqvist, U. Schroeder, and T. Mikolajick, *Advanced Functional Materials* **22**, 2412 (2012), ISSN 1616-3028, URL <http://onlinelibrary.wiley.com/doi/10.1002/adfm.201103119/abstract>.
 - [18] E. Yurchuk, J. Müller, S. Knebel, J. Sundqvist, A. P. Graham, T. Melde, U. Schröder, and T. Mikolajick, *Thin Solid Films* **533**, 88 (2013), ISSN 0040-6090, URL <http://www.sciencedirect.com/science/article/pii/S0040609012016264>.
 - [19] M. H. Park, H. J. Kim, Y. J. Kim, W. Lee, T. Moon, and C. S. Hwang, *Applied Physics Letters* **102**, 242905 (2013), ISSN 0003-6951, 1077-3118, URL <http://scitation.aip.org/content/aip/journal/apl/102/24/10.1063/1.4811483>.
 - [20] M. H. Park, H. J. Kim, Y. J. Kim, T. Moon, and C. S. Hwang, *Applied Physics Letters* **104**, 072901 (2014), ISSN 0003-6951, 1077-3118, URL <http://scitation.aip.org/content/aip/journal/apl/104/7/10.1063/1.4866008>.
 - [21] P. D. Lomenzo, P. Zhao, Q. Takmeel, S. Moghaddam, T. Nishida, M. Nelson, C. M. Fancher, E. D. Grimsley, X. Sang, J. M. LeBeau, et al., *Journal of Vacuum Science & Technology B, Nanotechnology and Mi-*

- croelectronics: Materials, Processing, Measurement, and Phenomena **32**, 03D123 (2014), ISSN 2166-2746, URL <http://avs.scitation.org/doi/10.1116/1.4873323>.
- [22] U. Schroeder, E. Yurchuk, J. Müller, D. Martin, T. Schenk, P. Polakowski, C. Adelmann, M. I. Popovici, S. V. Kalinin, and T. Mikolajick, Japanese Journal of Applied Physics **53**, 08LE02 (2014), ISSN 0021-4922, 1347-4065, URL <http://stacks.iop.org/1347-4065/53/i=8S1/a=08LE02?key=crossref.ad3265465d10aa004e56539e1d4feb68>.
- [23] M. H. Park, H. J. Kim, Y. J. Kim, W. Lee, T. Moon, and C. S. Hwang, Applied Physics Letters **105**, 072902 (2014), ISSN 0003-6951, URL <http://aip.scitation.org/doi/10.1063/1.4893376>.
- [24] X. Sang, E. D. Grimley, T. Schenk, U. Schroeder, and J. M. LeBeau, Applied Physics Letters **106**, 162905 (2015), ISSN 0003-6951, 1077-3118, URL <http://scitation.aip.org/content/aip/journal/apl/106/16/10.1063/1.4919135>.
- [25] M. Hoffmann, U. Schroeder, T. Schenk, T. Shimizu, H. Funakubo, O. Sakata, D. Pohl, M. Drescher, C. Adelmann, R. Materlik, et al., Journal of Applied Physics **118**, 072006 (2015), ISSN 0021-8979, 1089-7550, URL <http://scitation.aip.org/content/aip/journal/jap/118/7/10.1063/1.4927805>.
- [26] A. Chernikova, M. Kozodaev, A. Markeev, D. Negrov, M. Spiridonov, S. Zarubin, O. Bak, P. Buragohain, H. Lu, E. Suvorova, et al., ACS Applied Materials & Interfaces **8**, 7232 (2016), ISSN 1944-8244, URL <http://dx.doi.org/10.1021/acsami.5b11653>.
- [27] M. H. Park, T. Schenk, M. Hoffmann, S. Knebel, J. Gärtner, T. Mikolajick, and U. Schroeder, Nano Energy **36**, 381 (2017), ISSN 2211-2855, URL <http://www.sciencedirect.com/science/article/pii/S221128551730263X>.
- [28] M. H. Park, C.-C. Chung, T. Schenk, C. Richter, M. Hoffmann, S. Wirth, J. L. Jones, T. Mikolajick, and U. Schroeder, Advanced Electronic Materials **4**, 1700489 (2018), ISSN 2199-160X, URL <https://www.onlinelibrary.wiley.com/doi/abs/10.1002/aelm.201700489>.
- [29] R. C. Garvie, The Journal of Physical Chemistry **82**, 218 (1978), ISSN 0022-3654, URL <http://dx.doi.org/10.1021/j100491a016>.
- [30] K. Tomida, K. Kita, and A. Toriumi, Applied Physics Letters **89**, 142902 (2006), ISSN 0003-6951, URL <http://aip.scitation.org/doi/10.1063/1.2355471>.
- [31] T. S. Böske, P. Y. Hung, P. D. Kirsch, M. A. Quevedo-Lopez, and R. Ramirez-Bon, Applied Physics Letters **95**, 052904 (2009), ISSN 0003-6951, URL <http://aip.scitation.org/doi/10.1063/1.3195623>.
- [32] J. P. Perdew, K. Burke, and M. Ernzerhof, Physical Review Letters **77**, 3865 (1996), URL <http://link.aps.org/doi/10.1103/PhysRevLett.77.3865>.
- [33] D. Vanderbilt, Physical Review B **41**, 7892 (1990), URL <http://link.aps.org/doi/10.1103/PhysRevB.41.7892>.
- [34] P. Giannozzi, S. Baroni, N. Bonini, M. Calandra, R. Car, C. Cavazzoni, Davide Ceresoli, G. L. Chiarotti, M. Cococcioni, I. Dabo, et al., Journal of Physics: Condensed Matter **21**, 395502 (2009), ISSN 0953-8984, URL <http://stacks.iop.org/0953-8984/21/i=39/a=395502>.
- [35] N. Marzari, D. Vanderbilt, A. De Vita, and M. C. Payne, Physical Review Letters **82**, 3296 (1999), URL <http://link.aps.org/doi/10.1103/PhysRevLett.82.3296>.
- [36] L. Bengtsson, Physical Review B **59**, 12301 (1999), URL <http://link.aps.org/doi/10.1103/PhysRevB.59.12301>.
- [37] L. Bellaiche and D. Vanderbilt, Physical Review B **61**, 7877 (2000), URL <http://link.aps.org/doi/10.1103/PhysRevB.61.7877>.
- [38] Q. Zeng, A. R. Oganov, A. O. Lyakhov, C. Xie, X. Zhang, J. Zhang, Q. Zhu, B. Wei, I. Grigorenko, L. Zhang, et al., Acta Crystallographica Section C Structural Chemistry **70**, 76 (2014), ISSN 2053-2296, URL <http://scripts.iucr.org/cgi-bin/paper?S2053229613027861>.
- [39] S. E. Reyes-Lillo, K. F. Garrity, and K. M. Rabe, Physical Review B **90**, 140103 (2014), URL <http://link.aps.org/doi/10.1103/PhysRevB.90.140103>.
- [40] R. Materlik, C. Künneth, and A. Kersch, Journal of Applied Physics **117**, 134109 (2015), ISSN 0021-8979, 1089-7550, URL <http://scitation.aip.org/content/aip/journal/jap/117/13/10.1063/1.4916707>.
- [41] T. D. Huan, V. Sharma, G. A. Rossetti, and R. Ramprasad, Physical Review B **90**, 064111 (2014), URL <http://link.aps.org/doi/10.1103/PhysRevB.90.064111>.
- [42] R. Batra, T. D. Huan, G. A. Rossetti, and R. Ramprasad, Chemistry of Materials **29**, 9102 (2017), ISSN 0897-4756, URL <https://doi.org/10.1021/acs.chemmater.7b02835>.
- [43] M. Li, Z. Zhang, S. A. Campbell, W. L. Gladfelter, M. P. Agustin, D. O. Klenov, and S. Stemmer, Journal of Applied Physics **98**, 054506 (2005), ISSN 0021-8979, URL <https://aip.scitation.org/doi/10.1063/1.2039268>.
- [44] Z. Wang, W. G. Zhu, A. Y. Du, L. Wu, Z. Fang, X. A. Tran, W. J. Liu, K. L. Zhang, and H. Yu, IEEE Transactions on Electron Devices **59**, 1203 (2012), ISSN 0018-9383.
- [45] S. Starschich and U. Boettger, Journal of Materials Chemistry C **5**, 333 (2017), ISSN 2050-7534, URL <https://pubs.rsc.org/en/content/articlelanding/2017/tc/c6tc04807b>.
- [46] R. Batra, H. D. Tran, and R. Ramprasad, Applied Physics Letters **108**, 172902 (2016), ISSN 0003-6951, 1077-3118, URL <http://scitation.aip.org/content/aip/journal/apl/108/17/10.1063/1.4947490>.
- [47] D. Fischer and A. Kersch, Journal of Applied Physics **104**, 084104 (2008), ISSN 0021-8979, 1089-7550, URL <http://scitation.aip.org/content/aip/journal/jap/104/8/10.1063/1.2999352>.
- [48] C.-K. Lee, E. Cho, H.-S. Lee, C. S. Hwang, and S. Han, Physical Review B **78**, 012102 (2008), URL <http://link.aps.org/doi/10.1103/PhysRevB.78.012102>.
- [49] R. Batra, T. D. Huan, J. L. Jones, G. Rossetti, and R. Ramprasad, The Journal of Physical Chemistry C **121**, 4139 (2017), ISSN 1932-7447, URL <https://doi.org/10.1021/acs.jpcc.6b11972>.
- [50] M. W. Pitcher, S. V. Ushakov, A. Navrotsky, B. F. Woodfield, G. Li, J. Boerio-Goates, and B. M. Tissue, Journal of the American Ceramic Society **88**, 160 (2005), ISSN 1551-2916, URL <http://onlinelibrary.wiley.com/doi/10.1111/j.1551-2916.2004.00031.x/abstract>.
- [51] J. Chevalier, L. Gremillard, A. V. Virkar, and D. R. Clarke, Journal of the American Ceramic Society **92**, 1901 (2009), ISSN 1551-2916, URL <http://onlinelibrary.wiley.com/doi/10.1111/j.1551-2916.2009.03278.x/abstract>.

- [52] A. B. Mukhopadhyay, J. F. Sanz, and C. B. Musgrave, Physical Review B **73**, 115330 (2006), URL <http://link.aps.org/doi/10.1103/PhysRevB.73.115330>.
- [53] X. Luo, A. A. Demkov, D. Triyoso, P. Fejes, R. Gregory, and S. Zollner, Physical Review B **78**, 245314 (2008), URL <http://link.aps.org/doi/10.1103/PhysRevB.78.245314>.
- [54] X. Luo, W. Zhou, S. V. Ushakov, A. Navrotsky, and A. A. Demkov, Physical Review B **80**, 134119 (2009), URL <http://link.aps.org/doi/10.1103/PhysRevB.80.134119>.
- [55] V. Fiorentini and M. Methfessel, Journal of Physics: Condensed Matter **8**, 6525 (1996), ISSN 0953-8984, URL <http://stacks.iop.org/0953-8984/8/i=36/a=005>.
- [56] A. Eichler and G. Kresse, Physical Review B **69**, 045402 (2004), URL <http://link.aps.org/doi/10.1103/PhysRevB.69.045402>.

Supplementary Material for “Causes of ferroelectricity in HfO_2 thin films”

Mehmet Dogan^{1,2,3,4}, Nanbo Gong^{1,5}, Tso-Ping Ma^{1,5} and Sohrab Ismail-Beigi^{1,2,6,7}

¹Center for Research on Interface Structures and Phenomena, Yale University, New Haven, Connecticut 06520, USA

²Department of Physics, Yale University, New Haven, Connecticut 06520, USA

³Department of Physics, University of California, Berkeley, California 94720, USA

⁴Materials Science Division, Lawrence Berkeley National Laboratory, Berkeley, California 94720, USA

⁵Department of Electrical Engineering, Yale University, New Haven, Connecticut 06520, USA

⁶Department of Applied Physics, Yale University, New Haven, Connecticut 06520, USA

⁷Department of Mechanical Engineering and Materials Science, Yale University, New Haven, Connecticut 06520, USA

Oxygen coordination for dopants in HfO_2

We list the dopant-O distances for the nearest oxygens in the 3.125% doped HfO_2 for C, N, N* (N -1e), Al, Al* (Al +1e), Ti and Ge doping in table [S1](#); and for Sr, Sr* (Sr +2e), Y, Y* (Y +1e), La and La* (La +1e) doping in table [S2](#).

Phase	Nearest O neighbor distances (Å)								C. N.
mono C	1.28	1.31	1.36	2.67	2.70	2.74	2.85		3
ortho C	1.27	1.35	1.37	2.48	2.57	2.66	2.70		3
tetra C	1.45	1.45	1.45	1.45	2.86	2.86	2.86	2.86	4
mono N	1.26	1.31	1.71	2.62	2.79	2.85	2.96		2
ortho N	1.15	2.08	2.15	2.40	2.56	2.56	2.63		1
tetra N	1.24	1.24	1.95	2.18	2.74	2.74	2.75	2.76	2
mono N*	1.24	1.25	1.30	2.60	3.02	3.08	3.17		3
ortho N*	1.24	1.29	1.30	2.63	2.66	2.72	2.91		3
tetra N*	1.27	1.28	1.28	2.33	2.62	2.84	2.84	2.88	3
mono Al	1.87	1.92	1.95	2.03	2.06	2.16	2.81		5
ortho Al	1.91	1.96	1.97	2.00	2.01	2.09	2.79		5
tetra Al	1.83	1.83	1.83	1.83	2.64	2.64	2.64	2.64	4
mono Al*	1.88	1.94	1.95	2.04	2.06	2.19	2.82		5
ortho Al*	1.94	1.95	1.97	1.99	2.03	2.12	2.87		5
tetra Al*	1.83	1.83	1.83	1.83	2.71	2.71	2.71	2.71	4
mono Ti	1.92	1.96	2.06	2.07	2.10	2.25	2.27		5
ortho Ti	1.88	2.03	2.04	2.07	2.09	2.24	2.30		5
tetra Ti	1.88	1.88	1.88	1.88	2.58	2.58	2.58	2.58	4
mono Ge	1.88	1.88	1.94	1.95	1.99	2.22	2.84		5
ortho Ge	1.87	1.92	1.93	1.93	1.99	2.17	2.90		5
tetra Ge	1.81	1.81	1.81	1.81	2.69	2.69	2.69	2.69	4

Table S1: List of (C, N, N*, Al, Al*, Ti, Ge)-O bond lengths for each of the monoclinic, orthorhombic and tetragonal phases, for the 3.125% doped HfO₂. The number of oxygen neighbors to the dopant (coordination number) is reported in the rightmost column. It is assumed that if the distance between the two atoms is not much larger than the sum of their atomic radii, the two atoms are coordinated.

Phase	Nearest O neighbor distances (Å)								C. N.
mono Sr	2.31	2.31	2.33	2.43	2.43	2.43	2.46		7
ortho Sr	2.32	2.35	2.40	2.41	2.43	2.45	2.46		7
tetra Sr	2.38	2.38	2.38	2.38	2.50	2.50	2.50	2.50	8
mono Sr*	2.32	2.32	2.38	2.43	2.46	2.47	2.49		7
ortho Sr*	2.32	2.38	2.42	2.42	2.45	2.46	2.52		7
tetra Sr*	2.40	2.40	2.40	2.40	2.55	2.55	2.55	2.55	8
mono Y	2.17	2.19	2.27	2.27	2.29	2.34	2.36		7
ortho Y	2.18	2.24	2.27	2.27	2.29	2.33	2.36		7
tetra Y	2.24	2.24	2.24	2.24	2.42	2.42	2.42	2.42	8
mono Y*	2.17	2.19	2.27	2.28	2.30	2.35	2.37		7
ortho Y*	2.19	2.27	2.28	2.30	2.34	2.38	2.50		7
tetra Y*	2.24	2.24	2.24	2.24	2.44	2.44	2.44	2.44	8
mono La	2.23	2.25	2.34	2.35	2.36	2.40	2.44		7
ortho La	2.25	2.30	2.34	2.36	2.39	2.40	2.42		7
tetra La	2.31	2.31	2.31	2.31	2.47	2.47	2.47	2.47	8
mono La*	2.24	2.25	2.33	2.38	2.39	2.43	2.45		7
ortho La*	2.22	2.31	2.38	2.38	2.39	2.44	2.47		7
tetra La*	2.32	2.32	2.32	2.32	2.49	2.49	2.49	2.49	8

Table S2: List of (Sr, Sr*, Y, Y*, La and La*)-O bond lengths for each of the monoclinic, orthorhombic and tetragonal phases, for the 3.125% doped HfO₂. The number of oxygen neighbors to the dopant (coordination number) is reported in the rightmost column. It is assumed that if the distance between the two atoms is not much larger than the sum of their atomic radii, the two atoms are coordinated.

Energy vs matching area curves for (Al, Ge, Ti, La):HfO₂

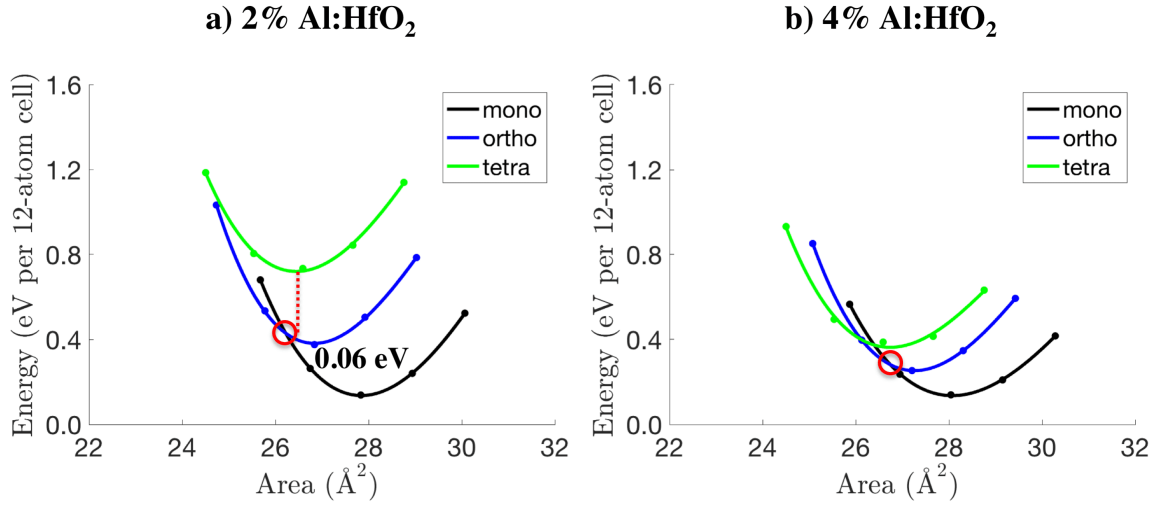


Figure S1: Energies of the monoclinic, orthorhombic and tetragonal phases vs in-plane matching area for epitaxially strained bulk simulations of (a) 2% Al doped and (b) 4% Al doped HfO_2 . For each composition and phase, five data points at -4%, -2%, 0%, 2% and 4% strain are chosen and computed (circular marks). The curves are obtained by fitting cubic polynomials to these five data points. The energy difference between the orthorhombic and the monoclinic phases at the optimized area of the t [100] grain is labelled in the figure in (a), and is equal to zero in (b). The zero of energy is chosen arbitrarily.

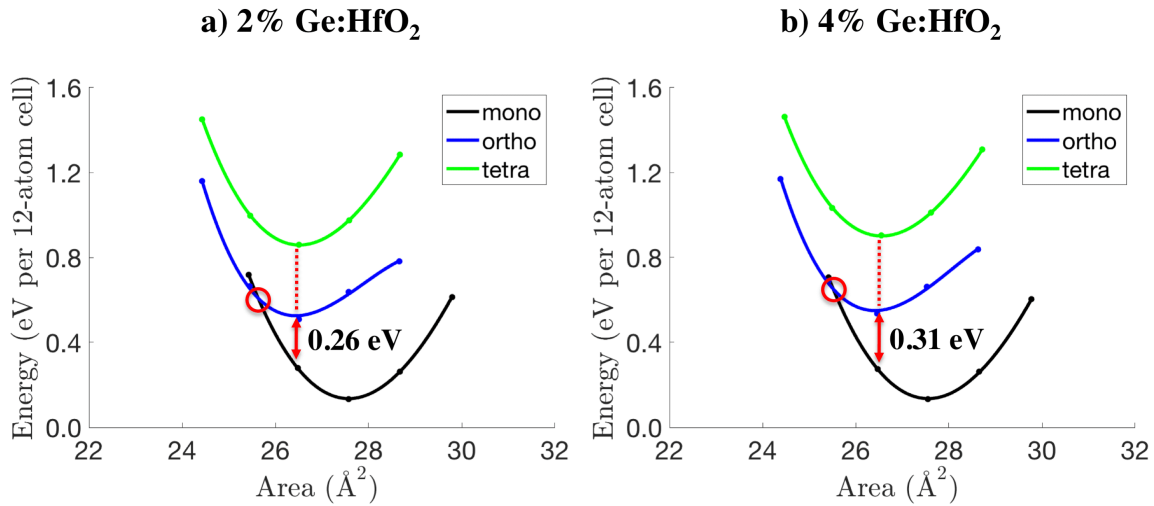


Figure S2: Energies of the monoclinic, orthorhombic and tetragonal phases vs in-plane matching area for epitaxially strained bulk simulations of (a) 2% Ge doped and (b) 4% Ge doped HfO_2 . For each composition and phase, five data points at -4%, -2%, 0%, 2% and 4% strain are chosen and computed (circular marks). The curves are obtained by fitting cubic polynomials to these five data points. The energy difference between the orthorhombic and the monoclinic phases at the optimized area of the t [100] grain is labelled in the figure. The zero of energy is chosen arbitrarily.

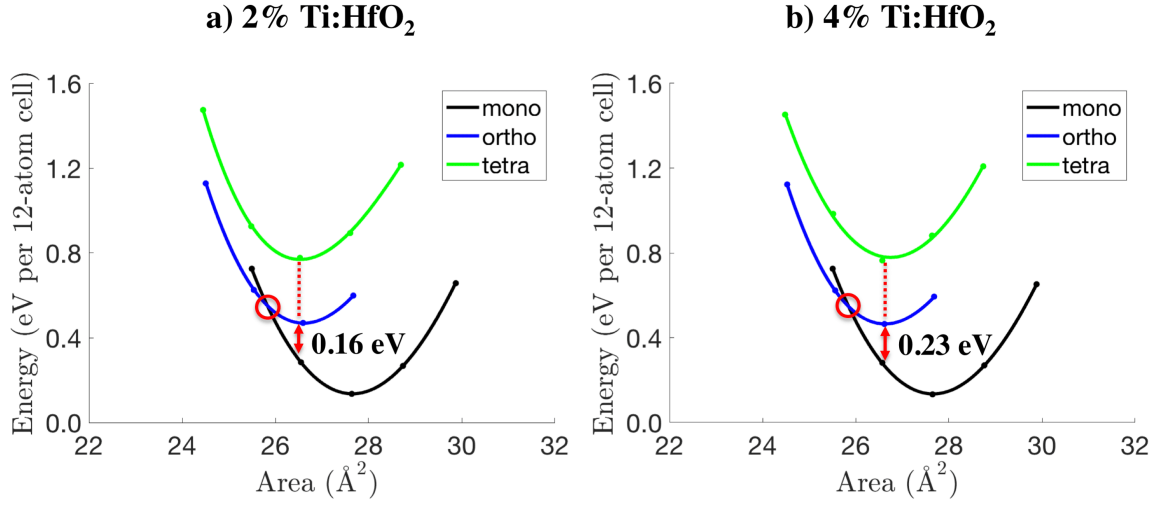


Figure S3: Energies of the monoclinic, orthorhombic and tetragonal phases vs in-plane matching area for epitaxially strained bulk simulations of (a) 2% Ti doped and (b) 4% Ti doped HfO_2 . For each composition and phase, five data points at -4%, -2%, 0%, 2% and 4% strain are chosen and computed (circular marks). The curves are obtained by fitting cubic polynomials to these five data points. The energy difference between the orthorhombic and the monoclinic phases at the optimized area of the t [100] grain is labelled in the figure. The zero of energy is chosen arbitrarily.

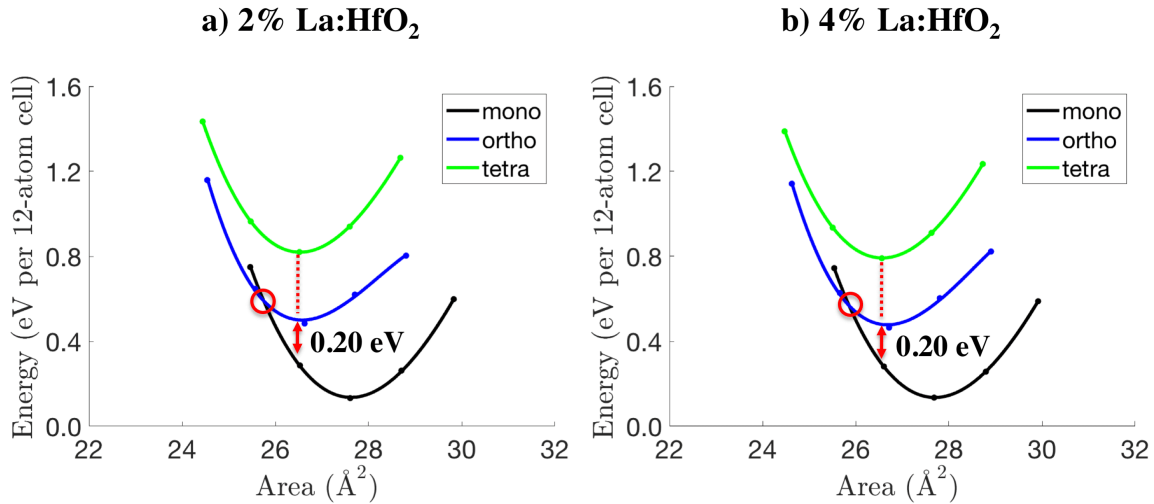


Figure S4: Energies of the monoclinic, orthorhombic and tetragonal phases vs in-plane matching area for epitaxially strained bulk simulations of (a) 2% La doped and (b) 4% La doped HfO_2 . For each composition and phase, five data points at -4%, -2%, 0%, 2% and 4% strain are chosen and computed (circular marks). The curves are obtained by fitting cubic polynomials to these five data points. The energy difference between the orthorhombic and the monoclinic phases at the optimized area of the t [100] grain is labelled in the figure. The zero of energy is chosen arbitrarily.